

Toward accurate and fast velocity quantification with 3D ultrashort TE phase-contrast imaging

Katja Degenhardt^{1,2}  | Simon Schmidt^{3,4}  | Christoph S. Aigner¹  |
 Fabian J. Kratzer⁴  | Daniel P. Seiter⁵ | Max Mueller⁶  | Christoph Kolbitsch¹  |
 Armin M. Nagel^{4,6}  | Oliver Wieben^{5,7}  | Tobias Schaeffter^{1,8,9}  |
 Jeanette Schulz-Menger^{10,11,12,13}  | Sebastian Schmitter^{1,3,4} 

Correspondence

Sebastian Schmitter,
 Physikalisch-Technische Bundesanstalt
 (PTB), Braunschweig and Berlin, Berlin,
 Germany.
 Email: sebastian.schmitter@ptb.de

Funding information

German Research Foundation,
 Grant/Award Numbers:
 GRK2260(BIOQIC), SCHM2677/4-1

Abstract

Purpose: Traditional phase-contrast MRI is affected by displacement artifacts caused by non-synchronized spatial- and velocity-encoding time points. The resulting inaccurate velocity maps can affect the accuracy of derived hemodynamic parameters. This study proposes and characterizes a 3D radial phase-contrast UTE (PC-UTE) sequence to reduce displacement artifacts. Furthermore, it investigates the displacement of a standard Cartesian flow sequence by utilizing a displacement-free synchronized-single-point-imaging MR sequence (SYNC-SPI) that requires clinically prohibitively long acquisition times.

Methods: 3D flow data was acquired at 3T at three different constant flow rates and varying spatial resolutions in a stenotic aorta phantom using the proposed PC-UTE, a Cartesian flow sequence, and a SYNC-SPI sequence as reference. Expected displacement artifacts were calculated from gradient timing waveforms and compared to displacement values measured in the in vitro flow experiments.

Results: The PC-UTE sequence reduces displacement and intravoxel dephasing, leading to decreased geometric distortions and signal cancellations in magnitude images, and more spatially accurate velocity quantification compared to the Cartesian flow acquisitions; errors increase with velocity and higher spatial resolution.

Conclusion: PC-UTE MRI can measure velocity vector fields with greater accuracy than Cartesian acquisitions (although pulsatile fields were not studied) and shorter scan times than SYNC-SPI. As such, this approach is superior to traditional Cartesian 3D and 4D flow MRI when spatial misrepresentations cannot be tolerated, for example, when computational fluid dynamics simulations are compared to or combined with in vitro or in vivo measurements, or regional parameters such as wall shear stress are of interest.

KEYWORDS

4D flow MRI, displacement artifact, flow artifact, GIRF, gradient imperfections, PC-UTE

Parts of this work have been presented at the 2022 Annual Meeting of the International Society for Magnetic Resonance in Medicine.

For affiliations refer to page 2006

This is an open access article under the terms of the [Creative Commons Attribution](https://creativecommons.org/licenses/by/4.0/) License, which permits use, distribution and reproduction in any medium, provided the original work is properly cited.

© 2024 Physikalisch-Technische Bundesanstalt (PTB) and The Authors. *Magnetic Resonance in Medicine* published by Wiley Periodicals LLC on behalf of International Society for Magnetic Resonance in Medicine.

1 | INTRODUCTION

Phase-contrast (PC) MRI has found widespread clinical use for the quantitative assessment of blood velocities and flow in the diagnosis of various cardiovascular diseases.¹ With the introduction of 4D flow MRI, the velocity vector field in an entire imaging volume can be captured throughout the cardiac cycle.^{2,3} These velocity measures provide the basis for comprehensive flow analysis and also enable the assessment of additional hemodynamic parameters such as pressure gradients,⁴ wall shear stress (WSS),⁵ kinetic energy,⁶ pulse wave velocity,⁷ vortex formation,^{8,9} and intracardiac flow component analysis.¹⁰ Such parameters can provide additional information for studying disease mechanisms, diagnosis, and treatment monitoring and planning.

4D flow MRI is also increasingly used for in vitro imaging of synthetic and biological flow phantoms, for example, to study underlying hemodynamic effects,^{11,12} assess accuracy and precision of PC MRI hemodynamic measures,¹³ predict surgical outcomes with rapid prototyping models,^{14,15} and evaluate computational fluid dynamics modeling results.¹⁶

Such in vitro scans offer advantages over in vivo scans, including prolonged scan times to support higher spatial/temporal resolutions and/or higher precision, controlled and repeatable acquisitions without motion artifacts, and comparisons with other velocity measures such as particle image velocimetry.^{17,18} Whereas several correction methods are routinely applied to PC MRI during image reconstruction and postprocessing¹⁹ to reduce errors due to eddy currents or concomitant fields, some other errors remain unaccounted for in traditional PC MRI. Notably, the non-zero TE causes intravoxel dephasing and associated signal voids; time differences between the spatial-encoding time points of different axes yield geometric *distortions* or *spatial displacements*²⁰; and time differences between spatial- and velocity-encoding time points lead to errors in the velocity maps when acceleration is present,^{21–24} sometimes denoted as *velocity displacements*.²⁰ These artifacts have already been reported in the early development stages of PC MRI^{22,23} but have received limited attention since the introduction of 4D flow MRI. However, they become of concern if spatial accuracy is of importance, for example, when (1) comparing MRI velocity fields with other spatially resolved measures such as particle image velocimetry,^{17,18} (2) merging data sets such as computational fluid dynamics and PC MRI for improved velocity fields data²⁵ or segmentations obtained from MR angiography or cardiac anatomy datasets with PC MRI for improved vessel boundary detections,²⁶ or (3) calculating stream-

lines along torturous vessel paths.²⁷ In addition, spatially sensitive measures such as WSS have been shown to be affected.²⁸

Different solutions have been proposed to counteract the displacements and geometric distortions in PC MRI. First, displacements can be partially corrected by estimating the actual location of affected voxels by reversing the displacement with a single step²⁰ or iterative solver²⁹ retrospectively during data processing. Second, geometric distortions caused by the non-synchronized position-encoding time points^{24,30} (t_i^0 , for axis $i = x, y, z$) have been reduced by changing the flow-encoding scheme from the fast but non-synchronous “Bernstein encoding scheme” designed to minimize TE³¹ to an echo-encoded scheme,^{23,32} in which the displacement is consistent along all three encoding directions, that is, $t_x^0 = t_y^0 = t_z^0$. This prospective solution, however, does not reduce the velocity displacement. In contrast, it often rather increases the displacement because of prolonged TEs. Third, the spatial shift as well as the geometric distortions are directly impacted by the choice of imaging parameters that affect the sequence timing parameters, including the chosen velocity-encoding sensitivity (VENC), sequence timing parameters, receiver bandwidth, and spatial resolution. Minimizing TE is not only beneficial for reducing intravoxel dephasing^{21,33} but also for reducing the time interval between position- and velocity-encoding ΔT_i^v along axis i , and thus the velocity displacement.³⁴

Another prospective solution for reducing geometric distortions, spatial and velocity displacements, is to change the type of sequence trajectory. Bruschewski et al. presented a SYNC-SPI (synchronized-single-point-imaging) sequence³⁵ that eliminates geometric distortions and displacements by simultaneously encoding the velocity and position on all axes. However, whereas the SYNC-SPI sequence provides highly accurate velocity vector fields, it acquires a single k-space point per repetition time, yielding extraordinarily long scan times of several hours up to several days that are often highly demanding concerning the stability of the flow setup and MRI system or even unfeasible. In practice, a faster method than the SYNC-SPI is often needed, but at the same time it should provide more accurate results than conventional Cartesian acquisitions and independence of the chosen orientation.

Using asymmetric Cartesian readout sampling schemes³⁶ can reduce ΔT_i^v , but still the artifacts are non-isotropic. Further shortening of ΔT_i^v can be achieved by readouts that start in the center of acquisition k-space, for example stack-of-stars^{37,38} or stack-of-spirals.^{34,39} It was shown that these sequences are beneficial for investigating complex flow in stenotic jets with high velocities^{34,38,39}

since short TE values reduce intravoxel dephasing and signal loss.

For magnitude-based applications, UTE sequences⁴⁰ combined with nonselective RF pulses have been proposed that use isotropic center-out acquisitions, for example, “kooshball”⁴⁰-like radial trajectories. Such radial UTE trajectories have also been used in combination with bipolar gradients for PC imaging, which has been termed PC-UTE. We adopt the term PC-UTE in this work, although an ultrashort TE value cannot be realized due to the flow-encoding gradient duration prior to the readout. In other works, 3D radial PC-UTE has been investigated in animal studies: improved velocity mapping compared to a corresponding Cartesian sequence was shown for self-gated 4D PC-UTE⁴¹ with a delayed readout gradient applied after the flow-encoding gradients. WSS values were derived from a self-gated 4D radial PC sequence⁴² utilizing an asymmetric readout. Further, peak flow and maximal velocities were obtained from accelerated 4D radial “center-out” PC data⁴³ utilizing compressed sensing with both readout gradients and data sampling delayed. Most of these works focused on the beneficial performance of radial center-out PC sequences regarding flow artifacts,^{41,43} robustness to motion,⁴³ and intravoxel dephasing.⁴¹ However, a thorough investigation of the associated displacement artifacts is lacking.

In this work, we investigate a 3D PC-UTE sequence and quantify its displacement artifact in an in vitro flow experiment. Comparison with a Cartesian PC sequence is performed, and SYNC-SPI data is acquired to serve as the ground truth. ΔT_i^v -values are calculated from the sequence timings for different spatial resolutions and image orientations, and displacement predictions from these calculated ΔT_i^v -values are compared to the measured values. Results obtained by the 3D PC-UTE sequence are compared to a Cartesian acquisition post-processed with the method proposed by Thunberg et al.²⁹ to correct the displacement artifacts.

2 | METHODS

2.1 | Calculation of encoding time points and displacement values

Although the position- and velocity-encoding process in PC MRI occurs within a finite duration, both processes are often considered to happen at single time points.^{24,30,31} For accurate flow encoding, the placement of these time points, that is, (t_x^0, t_y^0, t_z^0) for encoding the position along the x -, y -, and z -axis, as well as (t_x^1, t_y^1, t_z^1) for encoding the velocity along the axes, are essential.^{28,35,31,24} They

depend on various factors, including the sequence trajectory, image orientation, different (velocity) encoding schemes, gradient performance, and various sequence parameters such as receiver bandwidth, spatial resolution, and TE.

Along the readout (RO) direction³⁰ of a Cartesian sequence, for example, t_x^0 is considered to be located at the center of the echo and coincides with the center of the readout gradient for a symmetric readout (Figure 1). In contrast, if the fastest velocity encoding is implemented according to Bernstein et al.,³¹ t_y^0, t_z^0 along the phase encoding (PE) directions are located at the “gravity time point” of the applied PE gradients.²⁴ Thus, the time points t_i^0 are not synchronized between the axes, not only in the Cartesian case but also for other acquisitions such as stack-of-stars. As a result of this non-zero time interval $\Delta T_{ij}^0 = t_i^0 - t_j^0$ between position-encoding²⁴ and axes $ij = xy, xz, yz$, the position of moving spins appears spatially dislocated and can lead to geometric distortions.

In PC MRI, the time points for encoding the velocity are at the “gravity time point” of the bipolar gradient difference function.²⁴ In most sequences, the bipolar gradients are switched simultaneously (although potentially with different zeroth moments m_0 and first moments m_1) along the three axes; thus, the time points t_x^1, t_y^1, t_z^1 are typically close in time (Figure 1). However, there are time differences ΔT_i^v between t_i^1 and t_i^0 that can vary between the axes, with the readout axis typically showing the largest ΔT_{RO}^v . Since the velocity is encoded prior to the spatial position, the peak velocity in a stenotic region is shifted downstream. This velocity displacement Δd_i of moving spins with velocity component v_i and time interval ΔT_i^v along axis i is given by $\Delta d_i = v_i \cdot \Delta T_i^v$.

To investigate the dependency of the displacement artifacts on the spatial resolution and associated encoding time points, the Cartesian sequence is simulated with the vendor’s integrated development environment for applications (Siemens Healthineers, Erlangen, Germany, IDEA, version VB17) for isotropic resolutions ranging between 0.6 and 5.3 mm (TE = 5.4–2.8 ms), with otherwise identical settings (VENC: 2.5 m/s, receiver bandwidth: 450 Hz/Px, maximal gradient amplitude: 19.2 mT/m, and maximal gradient slew rate: 96 mT/m/ms). In the PC-UTE sequence, the time points t_i^1 and t_i^0 , as well as ΔT_{ij}^0 and ΔT_i^v , are not affected by changing the resolution or receiver bandwidth because the “center-out” sampling requires no m_0 for prewinding (Figure 1). Therefore, the radial sequence is simulated only once for an applied VENC of 2.5 m/s. From the obtained gradient waveforms, the encoding timepoints (t_i^1, t_i^0) and ΔT_i^v are derived and the expected velocity displacement values Δd_i calculated (Table 1).

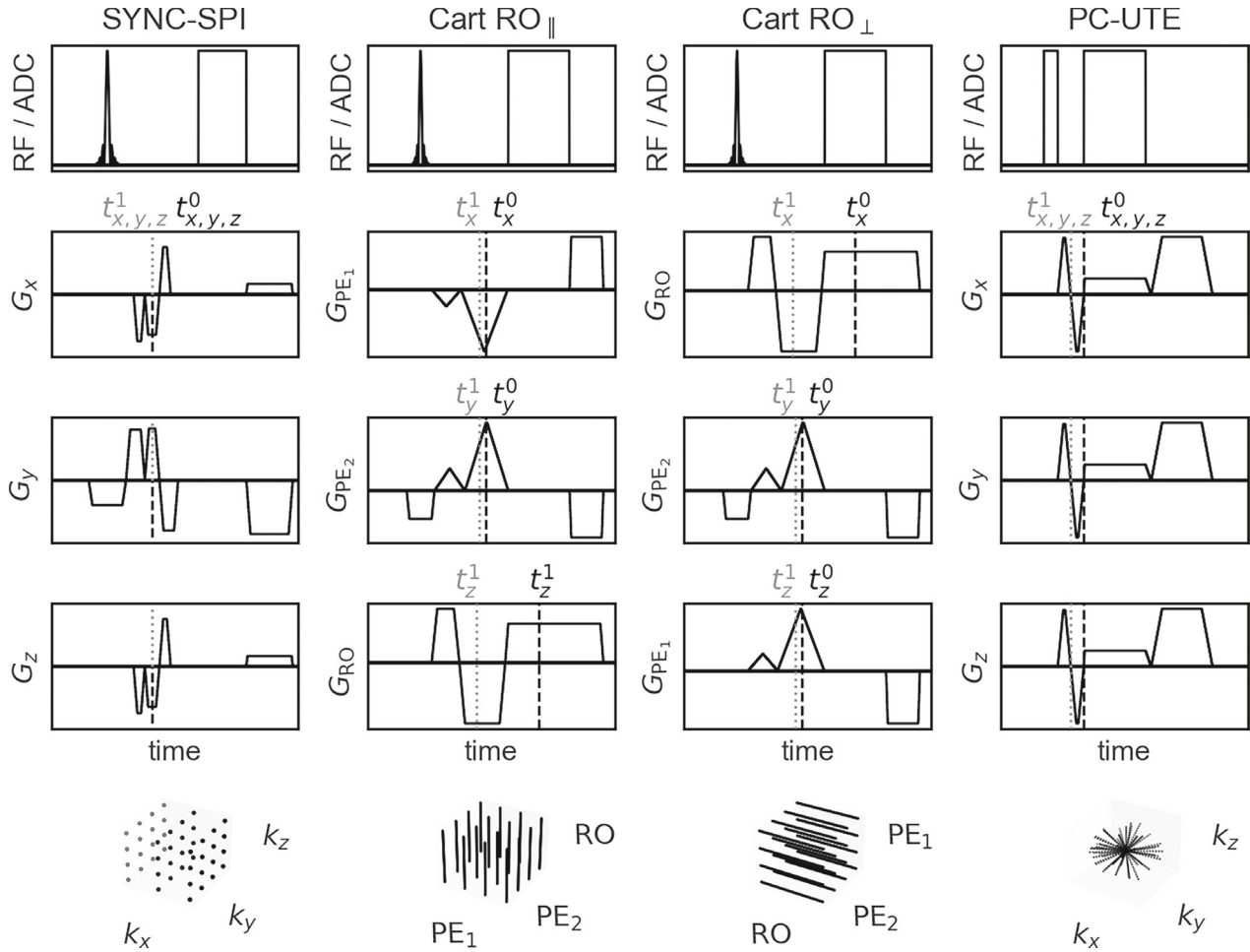


FIGURE 1 Sequence diagrams for flow acquisitions, exemplarily for one TR. From left to right: SYNC-SPI (reference),³⁵ Cartesian,³¹ and proposed 3D PC-UTE sequence. In Cart RO_{||}, RO, PE₁, PE₂ are played out on z-, x- and y-axis (RO parallel to z-axis). In Cart RO_⊥, RO, PE₁, PE₂ are played out on x-, z-, and y-axis (RO orthogonal to z-axis). Position-encoding time points (t_x^0, t_y^0, t_z^0) are marked by black dashed lines, and velocity-encoding time points (t_x^1, t_y^1, t_z^1) by gray dotted lines. Bottom row: a sketch of acquired data. PC, phase contrast; PE, phase encoding; RO, readout; SYNC-SPI, synchronized-single-point-imaging.

2.2 | Phase-contrast MRI sequences

In this work, three sequences as outlined in the following are used to investigate the displacement artifacts quantitatively.

2.2.1 | 3D Cartesian PC sequence

A Cartesian 3D PC MRI sequence is investigated, including different imaging orientations. The velocity-encoding gradients are implemented according to the established

TABLE 1 Calculated and measured displacement values Δd_z with corresponding time intervals ΔT_z^v of encoding directions played out along stenosis for flow experiments with constant flow rates $Q_1/Q_2/Q_3 = 40/30/20$ mL/s (corresponding to maximal expected velocities $v_z = 2.0/1.5/1.0$ m/s), VENC = 2.5 m/s, bandwidth = 450 Hz/Px, 1 mm isotropic resolution.

PC sequences	SYNC-SPI			Cart RO			Cart RO _⊥			PC-UTE		
ΔT_z^v (ms)	0.0			3.3			0.7			0.5		
Constant flow rate	Q₁	Q₂	Q₃	Q₁	Q₂	Q₃	Q₁	Q₂	Q₃	Q₁	Q₂	Q₃
Δd_z (calculated) (mm)	0.0	0.0	0.0	6.6	5.0	3.3	1.4	1.0	0.7	1.0	0.8	0.5
Δd_z (measured) (mm)	0.0	0.0	0.0	6.0	5.0	3.0	1.0	1.0	1.0	1.0	1.0	1.0

Abbreviations: PC, phase-contrast; RO, readout; SYNC-SPI, synchronized-single-point-imaging; VENC, velocity-encoding sensitivity.

method proposed by Bernstein et al.,³¹ providing the fastest encoding scheme and a minimal TE.³¹ Here, the m_0 of the pre-/rewinding gradients are included in the bipolar gradients for velocity encoding, yielding non-synchronized position- and velocity-encoding time points for the three individual axes (Figure 1). Consequently, ΔT_{ij}^0 and ΔT_i^v vary between axes resulting in both velocity displacements and geometric distortions.

2.2.2 | 3D PC-UTE sequence

3D velocity-encoding gradients with the shortest possible duration³¹ are integrated into a 3D UTE radial readout sequence⁴⁰ in which the readout starts in k-space center and subsequently moves radially outwards. A rectangular-shaped 500 μ s-long RF pulse is followed by bipolar gradients (total duration = 940 μ s for VENC = 2.5 m/s, TE = 1.2 ms), trapezoidal readout, and spoiling gradients (Figure 1). The first readout-spoke ends at the south pole (z -axis) and the ends of subsequent spokes spiral up to the north pole, while each TR is repeated four times with different velocity encodings. While the readout gradient changes direction, the four velocity-encoding gradients remain constant along the axes throughout the sequence.

Due to “center-out” acquisitions, the m_0 of the bipolar-encoding gradients vanishes. A two-sided velocity-encoding scheme³¹ is implemented with a constant absolute m_1 across all four flow encodes (FE) and all three directions (x , y , z) but with swapping signs: $m_1^{\text{FE } 1} = \left(-\frac{\Delta m_1}{2}, -\frac{\Delta m_1}{2}, -\frac{\Delta m_1}{2}\right)$, $m_1^{\text{FE } 2} = \left(+\frac{\Delta m_1}{2}, -\frac{\Delta m_1}{2}, -\frac{\Delta m_1}{2}\right)$, $m_1^{\text{FE } 3} = \left(-\frac{\Delta m_1}{2}, +\frac{\Delta m_1}{2}, -\frac{\Delta m_1}{2}\right)$, $m_1^{\text{FE } 4} = \left(-\frac{\Delta m_1}{2}, -\frac{\Delta m_1}{2}, +\frac{\Delta m_1}{2}\right)$. As a result, the velocity-encoding timepoints t_i^1 are synchronized for all three axes $i = x, y, z$. Additionally, the position-encoding timepoints t_i^0 are likewise synchronized, which eliminates geometric distortions, and are located at the beginning of the readout. Thus, this sequence shows a minimal time interval ΔT_i^v along all axes, resulting in an isotropic sensitivity to spatial displacements.

2.2.3 | SYNC-SPI

A SYNC-SPI sequence³⁵ is applied in addition to the other two acquisitions, which is regarded as a ground truth here. The SYNC-SPI achieves $\Delta T_{xy,xz,yx}^0 = \Delta T_{x,y,z}^v = 0$ for all three axes by synchronizing t_i^1 and t_i^0 , resulting in a single time point, that is, $t_x^0 = t_y^0 = t_z^0 = t_x^1 = t_y^1 = t_z^1$, preventing velocity displacements and geometric distortions. This is feasible because only a single point in k-space is acquired per TR, and the k-space position does not change

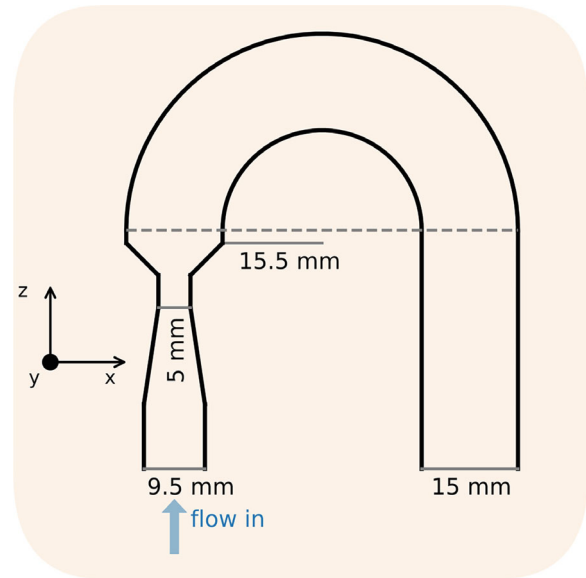


FIGURE 2 Sketch of stenotic flow phantom setup embedded in polyvinylpyrrolidone and positioned along physical scanner coordinates (x , y , z). The blue arrow marks the inflow direction.

during readout but it comes at the expense of approximately two orders of magnitude longer acquisition time, that is, multiple hours instead of a few minutes.

2.3 | Setup and flow measurements

In vitro flow experiments are performed on a 3T MR system (Siemens Verio, Erlangen, Germany) with a flow pump (CardioFlow 5000 MR, Shelley Medical Imaging Technologies, London, Canada) using three different constant flow rates $Q_1/Q_2/Q_3$ of 40/30/20 mL/s leading to maximal expected velocities of 2.0/1.5/1.0 m/s within the stenotic region of the flow phantom. Distilled water is pumped through the phantom consisting of a Venturi nozzle followed by a U-bend of 150 mm diameter (Figure 2) embedded in static 1.5% agarose gel, representing a stenotic aorta.²⁸ The flow phantom has an aortic diameter of 9.5 and 15.0 mm proximal and distal to the stenosis (Figure 2). Reynold numbers of approximately 2700/2000/1300 and 5100/3800/2500 are expected in the pipe inflow and the stenosis for $Q_1/Q_2/Q_3$, respectively.

All 3D flow sequences are acquired with non-time-resolved three-directional velocity encoding (3D PC MRI) using a 15-channel knee coil (QED, Mayfield Village, OH USA). For characterization of the MR gradient system and subsequent correction of the data due to deviations from the nominal radial readout trajectory, the gradient impulse response function (GIRF)⁴⁴ is measured using 12 triangular gradients (durations of 50–160 μ s) with a magnetic field camera (Skope Magnetic Resonance Technologies, Zurich, Switzerland) according to Vannesjo et al.⁴⁴

The flow phantom experiments are performed with the Cartesian, PC-UTE, and SYNC-SPI sequences for Q_1 , Q_2 , and Q_3 . While ΔT_{ij}^0 and ΔT_i^v are independent of the image orientation for the PC-UTE and SYNC-SPI, this is not the case for the Cartesian sequence. Hence, the Cartesian acquisitions were performed twice, first with readout-direction parallel (Cart RO_{\parallel}) and second with readout-direction perpendicular (Cart RO_{\perp}) to the stenosis. Figures 1 and 2 display all sequences for a single TR, with corresponding encoding time points and the phantom setup/geometry.

All flow sequences are acquired with a nominal 1 mm isotropic resolution and 12° flip angle. Imaging parameters for the PC-UTE scan are: FOV = $256 \times 256 \times 256$ [mm]³, 50000 spokes, TE/TR = 1.2/7.6 ms, nonselective excitation; for Cartesian scans: FOV = $256 \times 128 \times 60/256 \times 160 \times 60$ [mm]³ (Cart RO_{\parallel} /Cart RO_{\perp}), TE/TR = 4.3/7.1 ms, slab-selective excitation; and for SYNC-SPI scan: FOV = $256 \times 128 \times 26$ [mm]³, TE/TR = 2.2/7.1 ms, slab-selective excitation. All detailed measurement parameters are summarized in Table S1.

Additional Cartesian 3D flow acquisitions are performed with constant flow rate Q_1 and different isotropic resolutions (0.6/1.6/1.8/2.3/2.7 mm, TE = 5.6/3.8/3.6/3.5/3.5 ms) for Cart RO_{\parallel} and Cart RO_{\perp} to validate the displacement dependence on the resolution. All detailed measurement parameters are summarized in Table S2.

2.4 | Reconstruction and post-processing of velocity data

All datasets are reconstructed using custom-written reconstruction software in Python (version 3.7). To correct for gradient imperfections in the radial acquisitions, a GIRF⁴⁵ is applied to both the nominal bipolar and radial readout gradients. The radial datasets are then reconstructed with density compensation, and a nonuniform fast Fourier operator is applied to the GIRF-predicted k-space trajectory.

No Maxwell correction is applied throughout this work. Background phase correction using a third-order polynomial fit on static material (see Figure 2 for surrounding tissue) is applied for each velocity dataset, and the resulting fit is subtracted from the velocity maps.

2.5 | Data evaluation

2.5.1 | Velocity displacements

The highest velocity shifts within the phantom are expected in the stenotic region. To quantify the shift and

its dependence on the image orientation, the velocity component v_z along the stenosis is evaluated for $Q_1 - Q_3$ and all three acquisitions. For this, the v_z -component of the SYNC-SPI data is shifted by $v_z \cdot \Delta T_z^v$ for different ΔT_z^v -values. Since the expected displacement values are smaller than the acquired voxel size, the velocity data is first interpolated to a finer grid, shifted by amount ΔT_z^v , and then interpolated to the original voxel grid again. Subsequently, the correlation between the shifted SYNC-SPI and the other acquisitions is obtained. The ΔT_z^v with the best correlation to the measured v_z of Cart RO_{\parallel} , Cart RO_{\perp} , and PC-UTE is determined, and the measured velocity shift Δd_z for the velocities of 2.0/1.5/1.0 m/s is derived.

2.5.2 | Geometric distortions

Geometric distortions are present in both the magnitude and velocity maps due to non-zero and non-synchronized ΔT_{ij}^0 -values, which may result in the signal of moving spins being shifted into the walls of the vessel pipes. To visualize the geometric distortions in the velocity data, masks of the vessel boundaries are overlaid with the velocity maps for the different PC MRI acquisitions. Masks are obtained with the software ITK-SNAP (version 4.0.0) by applying seed points in the magnitude images for each acquisition. The shift of the fluid within the pipe is determined by comparing the masks to the SYNC-SPI-mask and the maximum shift distance is reported.

2.5.3 | Sensitivity to intravoxel dephasing

For acquisitions with high TE, intravoxel dephasing can lead to signal cancellations and dropouts, which may affect velocity quantification and derived parameters. To investigate the performance of the Cartesian, PC-UTE, and SYNC-SPI sequences regarding signal attenuations, signal intensities in the magnitude data are analyzed in a region of interest (ROI) of 16 voxels downstream of the stenosis, which present the largest decrease of signal intensities due to complex flow for $Q_1 - Q_3$. For all acquisitions, the signal intensities are normalized to the mean inflow signal prior to the stenosis. The largest signal dropouts downstream of the stenosis are compared to those of the SYNC-SPI data.

2.5.4 | Flow and velocity value evaluation

To investigate the performance of all flow sequences, both flow rate and velocity component values are investigated.

First, the mean velocities with SDs are determined within ROIs of 36/122/11 voxels at different cross-sectional areas (pipe inflow/outflow/stenosis) of the flow phantom and Q_1 . Volumetric flow rates are then derived by multiplying these areas with the mean velocities. The mean velocity component v_x with SD is determined in a ROI of 43 voxels for all acquisitions in the arc of the pipe. Since the radial data is more strongly affected by system imperfections compared to the Cartesian sequence, the velocity values of v_z along a velocity line are investigated for the PC-UTE sequence regarding the performance of GIRF and background phase corrections.

2.5.5 | Retrospective displacement correction method

A retrospective correction method proposed by Thunberg et al.²⁹ is implemented and applied to both the velocity and magnitude data obtained with Cart RO_{||} and flow rate Q_1 , for which the displacement is most prominent along the z -axis. As described by Thunberg et al., the velocity values in the acquired data are set back by the displaced distance given by the velocity values multiplied by the time interval ΔT_{RO}^v . From this corrected velocity field, streamlines are calculated and tracked over ΔT_{RO}^v . The displaced velocities are then shifted backward from the end to the starting position of the streamlines, resulting in a further corrected velocity field. This process is repeated iteratively several times, including streamline calculation based on the new corrected velocity fields.

3 | RESULTS

3.1 | Calculation of encoding time points and displacement values

In Figure 3A–C, bipolar gradients with corresponding encoding time points and time intervals (shaded region) are displayed for one flow encode for the Cartesian and PC-UTE sequence as used in the measurements for a 1 mm isotropic resolution. The Cartesian encoding resulted in predicted values ΔT_z^v of 3.3 ms for the readout and 0.7 ms for the first PE direction. For the PC-UTE sequence, an isotropic value of $\Delta T_i^v = 0.5$ ms was calculated for all three spatial axes. With these time intervals, displacement values Δd_z of 6.6/5.0/3.3 mm for Cart RO_{||}, 1.4/1.0/0.7 mm for Cart RO_⊥, and 1.0/0.8/0.5 mm for PC-UTE were calculated for the three maximum velocities of $Q_1/Q_2/Q_3$, respectively. Calculated displacement values and corresponding time intervals are listed in Table 1.

Figure 3D–F illustrates the absolute displacement in mm as a function of the resolution, which was calculated for the three different sequences with VENC = 2.5 m/s. The SYNC-SPI shows no displacement independently of the resolution and for all axes. For the Cartesian sequence, the displacement depends on the spatial resolution, encoding axis, and velocity direction. The displacement along Cartesian readout dominates for a velocity of 2.0 m/s, increasing from 5.5 to 8.1 mm for isotropic resolutions of 2.0 and 0.6 mm, respectively. This effect becomes even more apparent when calculating the shift relative to the voxel size, as shown in Figure 3G–I. Here, the displacement increases from 2.7 to 13.4 voxels. For the PC-UTE, the calculated displacement is independent of both the direction and resolution but shows a non-zero value of 1.0 mm for a velocity of 2.0 m/s.

3.2 | Flow measurements

For the four flow acquisitions, the magnitude maps for Q_1 (Figure 4A) and velocity maps for the z -component of all three flowrates $Q_1 - Q_3$ (Figure 4B–D) are displayed in Figure 4. For each flow rate, all three velocity components and magnitude maps are displayed in Figures S1–S4 for the same slices. The displacement shifts and geometric distortions are less prominent with smaller flow rates and correspondingly smaller velocity values.

3.2.1 | Velocity displacements

The largest displacement occurs in Cart RO_{||} since the readout axis is aligned along the highest velocity component v_z (marked by gray arrow in Figure 4). For $Q_1 - Q_3$, the velocities along the dashed white line (Figure 5B) are displayed in Figure 6 to investigate the velocity shifts. Measured velocity displacement Δd_z resulted in 6.0/5.0/3.0 mm for Cart RO_{||}, in 1.0/1.0/1.0 mm for Cart RO_⊥, and in 1.0/1.0/1.0 mm for PC-UTE compared to the SYNC-SPI acquisition for $Q_1/Q_2/Q_3$, respectively. Cart RO_⊥ and PC-UTE show similar results for $Q_1 - Q_3$ (Figure 6).

In Figure S5, slices with sagittal orientations show similar results compared to slices with coronal orientations (Figure 4), depicting the dependence of the artifact in 3D volume. The dependence of the displacement on the acquired resolution of Cart RO_{||} and Cart RO_⊥ is illustrated in Figures S6 and S7. Velocity shifts of Cart RO_{||} compared to Cart RO_⊥ resulted in 9/2/2/1/1 voxels corresponding to 5.4/3.2/3.6/2.3/2.7 mm for the isotropic resolutions 0.6/1.6/1.8/2.3/2.7 mm.

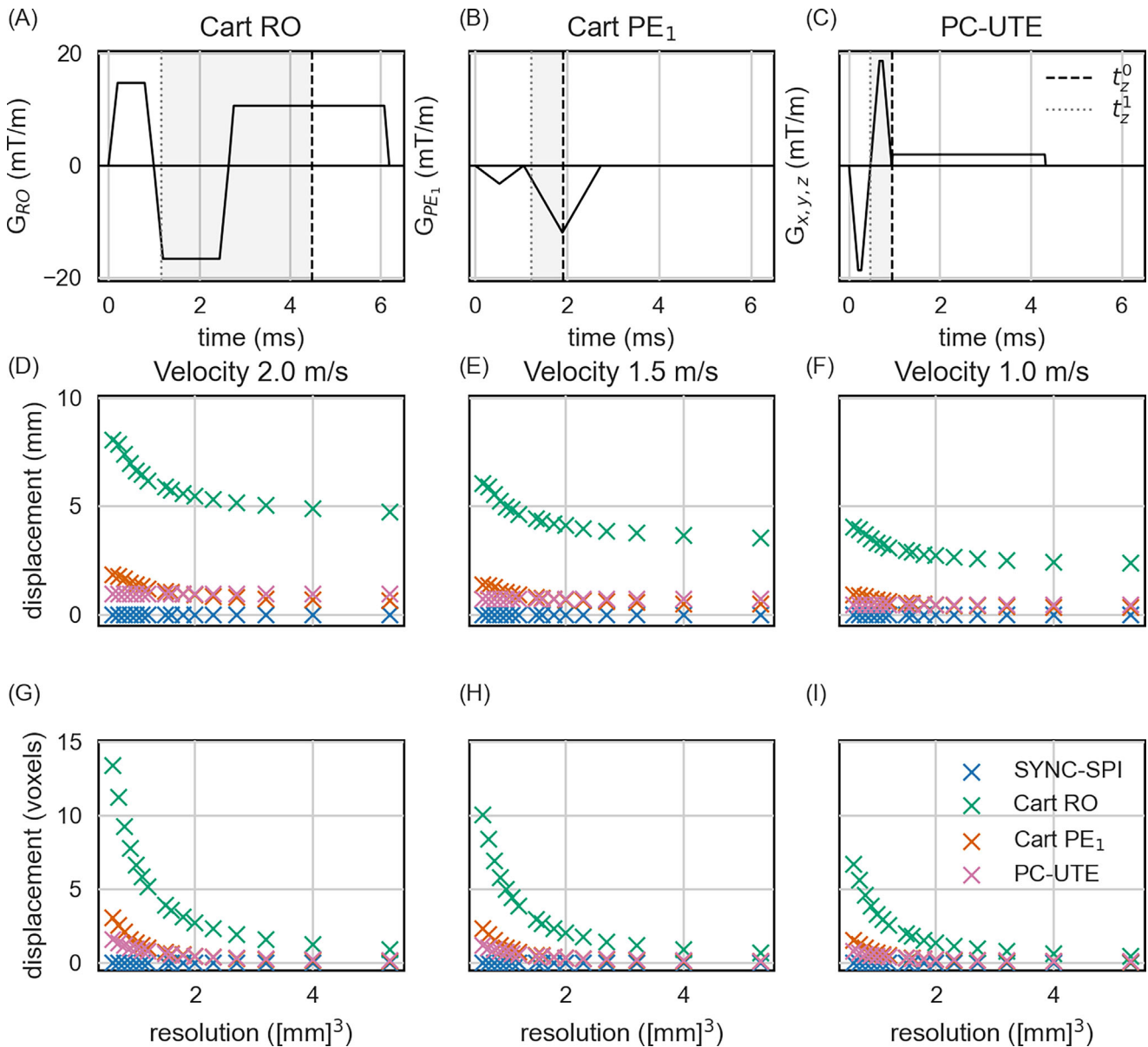


FIGURE 3 Gradient waveforms of bipolar gradients for Cartesian RO direction (A), Cartesian PE₁-axis (B), and PC-UTE sequence (C) (VENC = 2.5 m/s, bandwidth = 450 Hz/Px, 1 mm isotropic resolution). Readout gradients are displayed in (A) and (C). The position-encoding time points (t_z^0) are marked by black dashed lines, the velocity-encoding time points (t_z^1) by gray dotted lines. The gray shaded regions mark the time interval ΔT_z^v between t_z^1 and t_z^0 . Dependence of velocity displacement on isotropic resolution (range: 0.6–5.3 mm) in mm (D–F) and in number of voxels (G–I) for a flow velocity of 2.0/1.5/1.0 m/s. The larger displacement for Cart PE₁ for higher resolutions is caused by increasing area and length of the bipolar gradients along PE-axis with decreasing resolution; t_z^0 (located at “gravity time point”²⁴ of the second lobe) is more affected than t_z^1 (located at “gravity time point” of bipolar gradient difference, that is, more toward the beginning of second lobe). All flow sequences were calculated with the vendor’s integrated development environment for applications. VENC, velocity-encoding sensitivity.

3.2.2 | Geometric distortions

In Figure 4, the SYNC-SPI and PC-UTE data show no geometric distortions. However, in both Cartesian acquisitions, geometric distortions are observed. White arrows pointing to the pipe bending indicate the dependency of the distortions on the imaging axes in Figure 4. For Cart RO_{||}, with the readout direction applied along

the bottom–top direction, the signal of the moving fluid within the pipe is shifted 2–3 mm upward such that the wall appears to be thinner. Since the velocity component v_z shows a range of different values, moving spins are shifted by varying amounts. If the readout direction is oriented along the left–right direction (Cart RO_⊥), the moving fluid is shifted toward the right within the arch, and the pipe wall appears 2–3 mm broader compared to the SYNC-SPI.

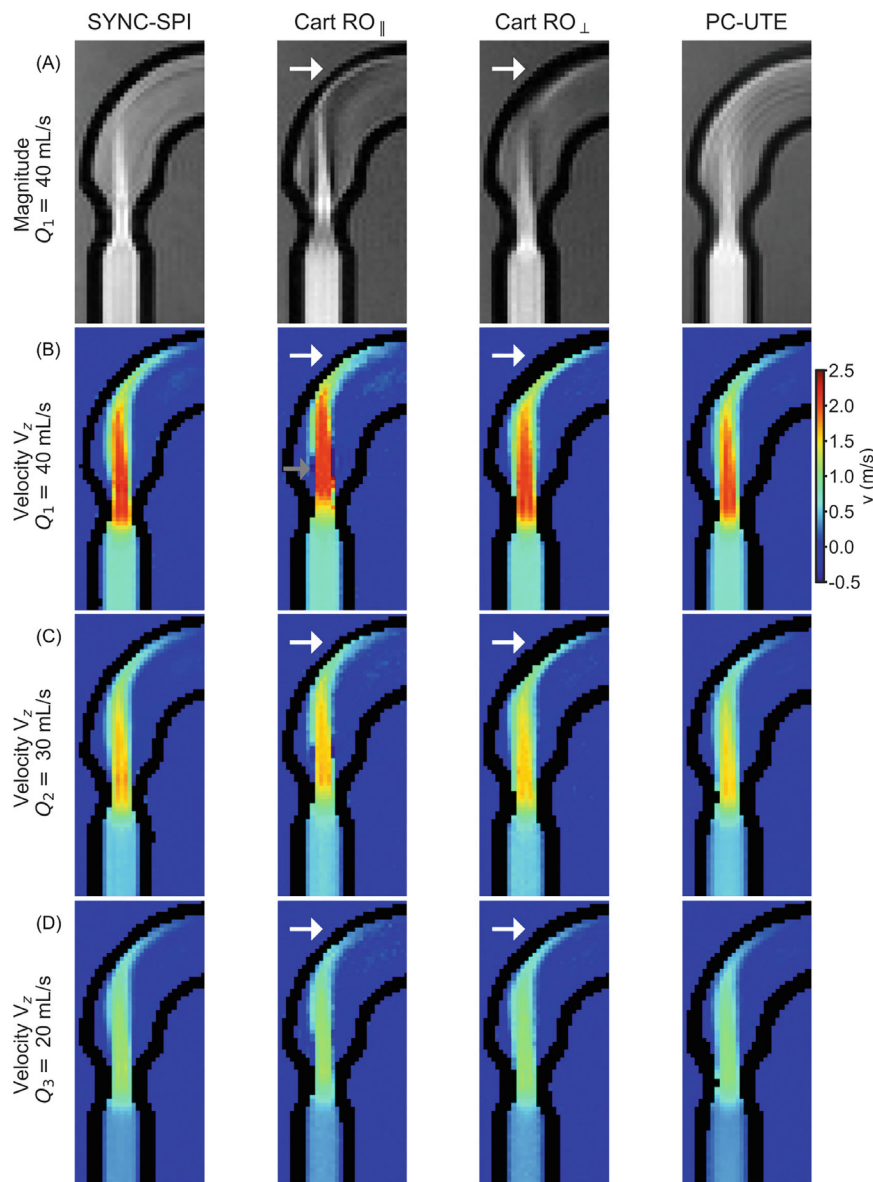


FIGURE 4 3D flow measurements in a stenotic flow phantom with $VENC = 2.5$ m/s and flow rates $Q_1 - Q_3$. (A) displays magnitude images of Q_1 , (B–D) the velocity maps of the velocity along the stenosis (v_z) for each flow rate. White arrows mark geometric distortions in both magnitude and velocity maps. Gray arrow mark velocity displacement mostly present in the velocity map v_z of Cart $RO_{||}$. Slices 9, 20, 38, 120 are displayed for SYNC-SPI, Cart $RO_{||}$, Cart RO_{\perp} , and PC-UTE, respectively.

3.2.3 | Sensitivity to intravoxel dephasing

Intravoxel dephasing can lead to signal cancellations in both velocity and magnitude maps. Whereas the SYNC-SPI shows the fewest signal fluctuations, both Cartesian acquisitions show a substantial signal loss in the magnitude images (black regions in Figure 5A), which correspond to complex flow regions and can be reduced by shortening TE. Signal intensities evaluated along the dashed white line in Figure 5A are displayed in Figure 7 for $Q_1 - Q_3$. The signal intensity decreased maximally by 92%/64%/23% (Q_1), 78%/42%/19% (Q_2), and 51%/25%/20% (Q_3) for Cart $RO_{||}$ /Cart RO_{\perp} /PC-UTE compared to the SYNC-SPI.

Signal dropouts do not only become apparent in the coronal view shown in Figure S4 but also in magnitude maps with sagittal orientations as depicted in Figure S5.

Additionally, the dependence of signal cancellations for different resolutions, and thus TE values, is illustrated in Figure S6. For the highest resolution (0.6 mm^3), signal cancellations are mostly prominent and decrease for lower resolutions ($>1.0 \text{ mm}^3$).

3.2.4 | Flow and velocity value evaluation

Mean velocity and volumetric flow rates are obtained for different cross-sections of the flow phantom for Q_1 (Figure S8). In the region of the stenosis, volumetric flow rates are underestimated by 47%/5%/10% for Cart $RO_{||}$ /Cart RO_{\perp} /PC-UTE compared to the SYNC-SPI. The high underestimation in Cart $RO_{||}$ demonstrates the velocity displacement of high velocities shifted downstream of the stenosis. The velocity component v_x

FIGURE 5 Zoomed magnitude (A) and velocity maps (B) downstream of the stenosis exemplarily for flow rate Q_1 . Signal cancellations in (A) are evaluated along the white dashed line in Figure 7. Velocity displacement shifts of highest velocities marked by white lines in (B), evaluation of velocities along the white dashed line in Figure 6. The velocity colormap corresponds to Figure 4.

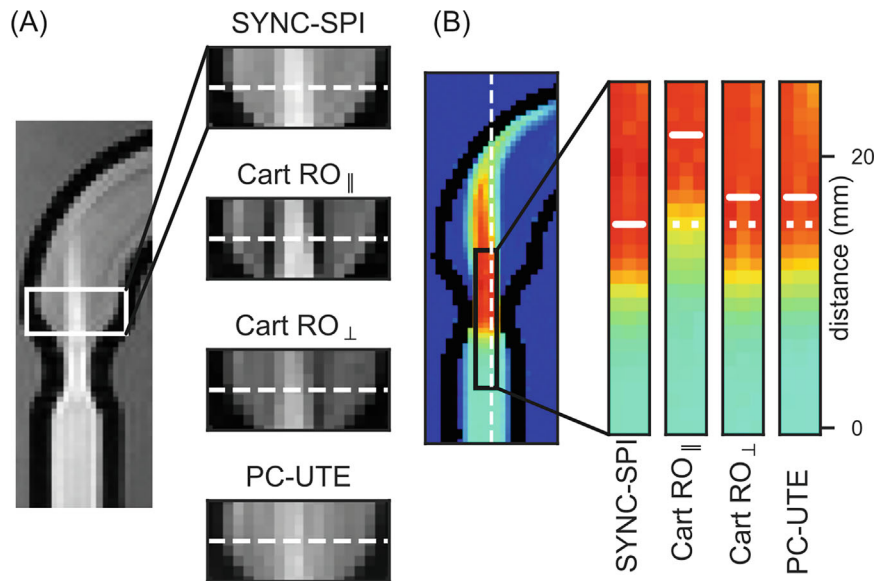
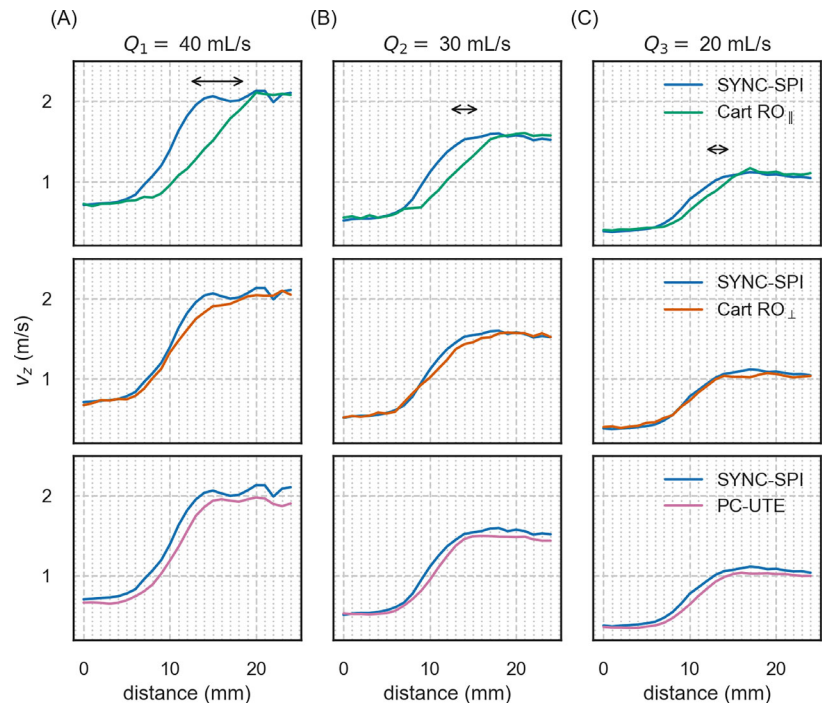


FIGURE 6 Quantification of velocity displacements in (A–C) corresponding to flow rates $Q_1 - Q_3$. Velocity components v_z are plotted along the dashed white line in Figure 5 for four acquisitions. Black arrows mark the large displacement of Cart RO_{||} acquisition (RO; Cart RO_⊥ and PC-UTE show similar performance).



was evaluated for all four acquisitions in the bending of the pipe and resulted in $-0.20 \pm 0.01 / -0.26 \pm 0.01 / -0.23 \pm 0.01 / -0.22 \pm 0.01$ m/s (Q_1), in $-0.21 \pm 0.01 / -0.20 \pm 0.01 / -0.15 \pm 0.01 / -0.17 \pm 0.01$ m/s (Q_2), and in $-0.13 \pm 0.01 / -0.11 \pm 0.01 / -0.12 \pm 0.01 / -0.14 \pm 0.01$ m/s (Q_3) for SYNC-SPI/Cart RO_{||}/Cart RO_⊥/PC-UTE, respectively. The velocity component v_y of PC-UTE shows an overall similar velocity pattern to the SYNC-SPI data (Figures S1–S3), whereas Cart RO_{||} and Cart RO_⊥ show deviations in the pipe-bending region, which may result from nonsynchronized position-encoding time

points in 3D volume. The velocity component v_z of the PC-UTE acquisition is displayed for the nominal and the GIRF-corrected trajectories as well as after background phase correction in Figure S9.

3.2.5 | Retrospective displacement correction method

The velocity and magnitude maps obtained after applying the correction method²⁹ on data acquired with Cart RO_{||}

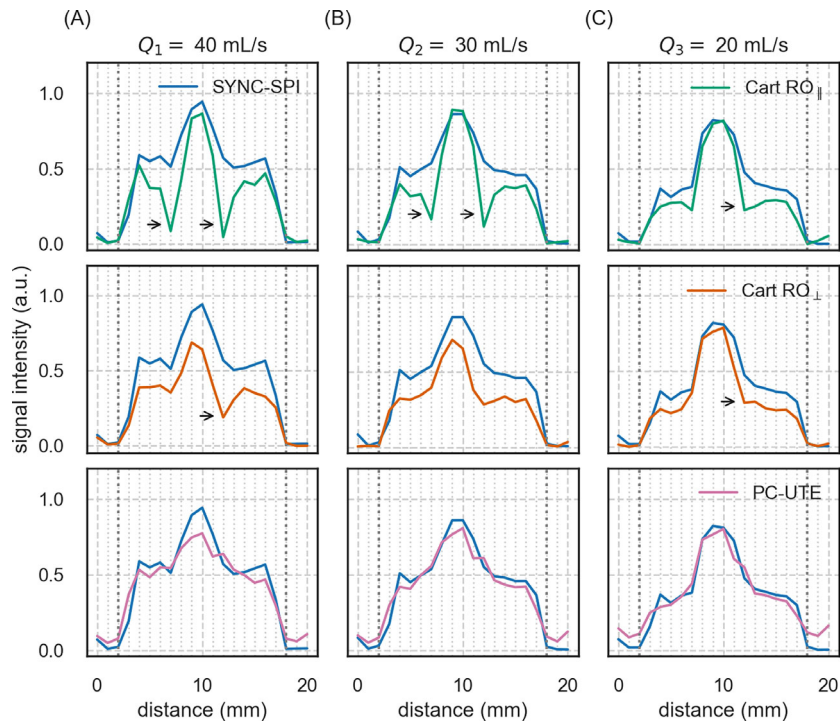


FIGURE 7 Quantification of signal intensities from magnitude maps for SYNC-SPI, Cart RO_{||}, Cart RO_⊥, and PC-UTE in (A–C) corresponding to flow rates $Q_1 - Q_3$. Signal intensities are plotted along the dashed white line in Figure 5; black arrows mark signal dropouts; and dotted black lines mark pipe edges.

are displayed in Figure 8. Displaced velocities (v_z) are successfully shifted backward (Figure 8C). The resulting shift with Cart RO_{||} obtained after correction deviates less than 1 mm to Cart RO_⊥, PC-UTE, as well as SYNC-SPI. However, the corrected velocity values do not completely match with the SYNC-SPI data. The signal of displaced spins is successfully shifted backward. Nevertheless, this correction method does not remove signal cancellations due to intravoxel dephasing.

4 | DISCUSSION

In this work, a 3D PC-UTE flow sequence was developed and investigated in *in vitro* flow experiments with a focus on displacement artifacts and intravoxel dephasing. To the best of our knowledge, it is the first report in the literature that quantitatively analyzes the displacement artifact with a PC-UTE sequence and compares it to both the displacement of a Cartesian and ground truth SYNC-SPI sequence.

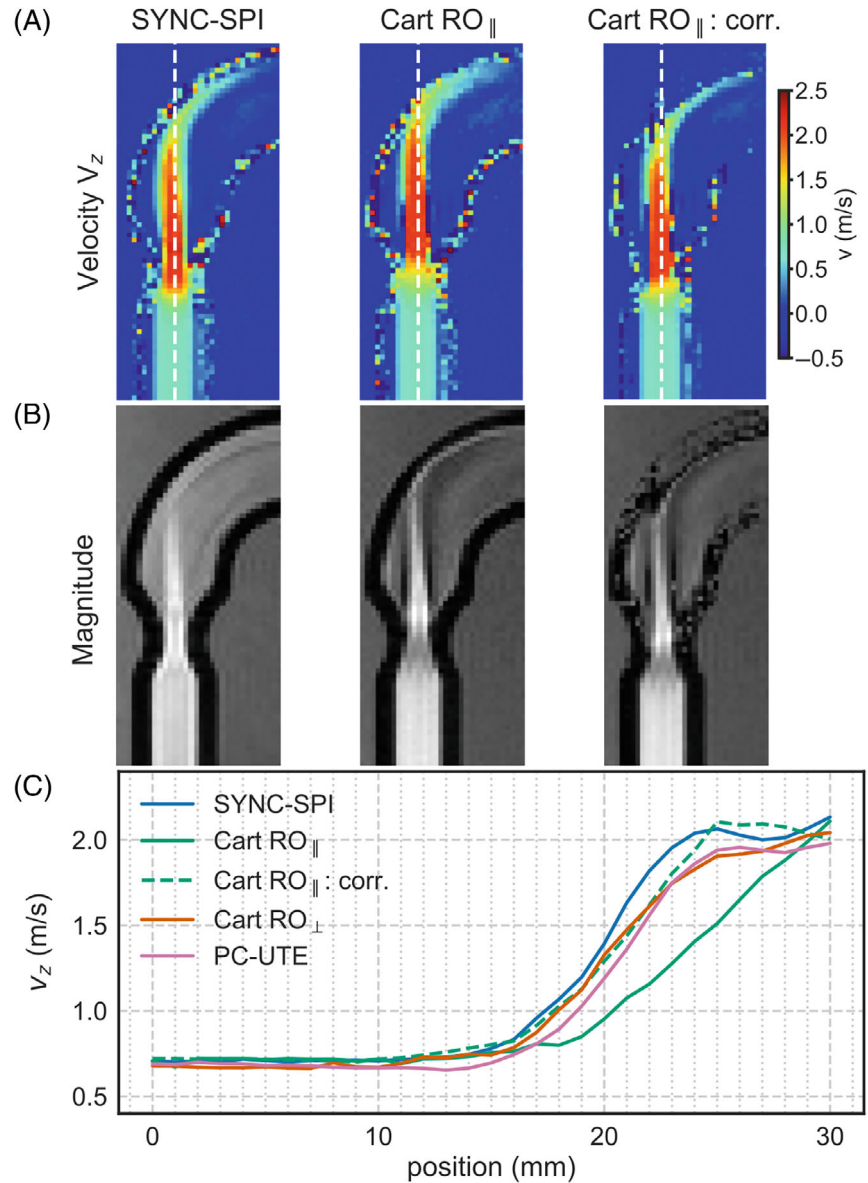
Over the past decade, the increasing availability of 4D flow sequences, post-processing packages, and 3D printers has led to a rising number of *in vitro* PC flow imaging studies investigating flow patterns and hemodynamic parameters in replicas of healthy and diseased vessels in detail. This approach enables analyzing the impact of specific anatomic features on the underlying flow pattern. It enables prolonged scan times not feasible in *in vivo* studies, thus supporting higher spatial resolutions.

However, applying Cartesian-based, PC flow sequences or PC sequences with long TE values for high-resolution applications yields strong spatial and/or velocity displacement artifacts,^{20,28} which can vary between the readout and PE axes.^{22,28} These effects impact spatial accuracy as well as measured velocity amplitudes, velocity vector fields, and derived hemodynamic parameters such as the WSS²⁸ and kinetic energy.

For the proposed PC-UTE sequence, ΔT_i^v only depends on the VENC value and gradient performance. Thus, newer MR systems with higher gradient performance are favorable for achieving shorter ΔT_i^v durations. In addition, the resolution and the receiver bandwidth impact the displacement for Cartesian sequences. For many flow applications, particularly for WSS estimation, high resolutions are required for obtaining accurate values.⁴⁶ Relative to the voxel size, the displacement increases disproportionately high, as shown in Figure 3E–I, demonstrating the importance of sequences that minimize those effects when high spatial resolutions are indispensable. As shown by Schmidt et al.,²⁸ varying WSS values are obtained from velocity fields acquired with either “Bernstein encoding scheme”^{28,31} ($t_x^0 \neq t_y^0, t_z^0$) or a scheme that synchronizes t_i^0 for all axes at TE²⁸ ($t_x^0 = t_y^0 = t_z^0$). Since the velocity-encoding scheme in our PC-UTE sequence eliminates ΔT_{ij}^0 and minimizes ΔT_i^v , WSS values derived from this acquisition are expected to be closer to the ground truth due to smaller and isotropic velocity shifts.

Synchronized encoding and vanishing ΔT_{ij}^0 and ΔT_i^v values are achievable by the SPRITE⁴⁷ or SYNC-SPI³⁵

FIGURE 8 Retrospective correction²⁹ of velocity data for Cart RO_{||} acquisition (“Cart RO_{||}: corr”) applied on (A) velocity component along the stenosis (v_z) and (B) magnitude for flow rate Q_1 , VENC = 2.5 m/s. In (C), velocities along the dashed line in (A) are displayed. Slices 9 and 20 are displayed for SYNC-SPI and Cart RO_{||}.



method, but they come at the cost of extensively long scan times. Different types of multi-slice 2D PC-UTE^{34,38,39} acquisitions have been investigated for flow imaging and can serve as a tradeoff between reduced scan time over point-based methods and greater accuracy over Cartesian acquisitions.

The PC-UTE scan time is substantially shorter than the SYNC-SPI counterpart but still requires around 25 min in the present implementation, which is 38% longer than the Cartesian scan time. Extending the technique toward 4D flow, including temporal dimensions, is straightforward but further prolongs the scan time. Nevertheless, radial acquisition schemes are well suitable for subsampling⁴⁸ and iterative reconstructions,⁴³ which have not been applied here.

Importantly, UTE sequences also reduce intravoxel dephasing, which was particularly beneficial in complex

flow.^{39,49} In this regard, center-out sampling strategies such as a center-out radial “kooshball”^{41,40,50} or cones⁵¹ are preferred for 3D PC imaging. Magnitude and velocity maps show fewer signal cancellations in stenotic regions due to shorter TE, which can be beneficial for quantification of turbulences.

Non-Cartesian UTE acquisitions, however, are susceptible to system imperfections.⁵² Gradient delays and trajectory deviations⁵² must be carefully considered and corrected during reconstruction. We chose the GIRF prediction model⁴⁴ to correct for gradient deviations. Correcting for both bipolar and readout gradients included the different polarities of the flow-encoding gradients in front of the radial readout for each flow encode. Eddy currents from the flow-encoding gradients that influence the readout could be mitigated, for example, by delaying the readout; but this would come at the expense of a prolonged

ΔT_i^y . Further investigations need to be carried out on the performance of the applied GIRF model, for example, by measuring the gradients directly with a field camera.

Measurements with varying flow rates demonstrated the linear dependency of the displacement on the velocity values. Consequently, a lower flow rate results only in moderate displacements. Thus, for pulsatile flow, which was not investigated in this work, only minor differences in the velocity displacements between the proposed PC-UTE and Cart RO_{||} are expected for the diastolic phase, whereas larger differences are expected in the systolic phase. Moreover, applying a smaller VENC value for better velocity-to-noise ratio typically increases TE and the length of the bipolar velocity-encoding gradients, thus the risk for geometric distortions and velocity displacements. Moreover, the artifact depends on the underlying geometry; for example, velocity shifts are visible in regions with acceleration and the shift occurs in the 3D volume. Note that geometric distortions also exist in non-PC MRI sequences, which can become important if images from different sequences are merged, for example, if a vessel segmentation for PC MRI is performed on a sequence different from the PC MRI sequence.

Applying the correction method²⁹ on the Cartesian data successfully shifted high velocities backward. However, signal dropouts that occur in regions downstream of the stenosis could not be retrieved. For the future, further improvements might be achieved by applying a mask of static tissue, preventing the signal from being shifted into the velocity fields.

5 | CONCLUSION

Due to the shortened and directionally independent time interval between spatial- and velocity-encoding, PC-UTE sequences are highly suitable for measuring the underlying velocity vector field more accurately compared to the Cartesian counterpart and in shorter scan times compared to sequences without displacement artifacts. This benefit becomes especially important when high resolution is desired or when imaging high flow velocities. The proposed 3D PC-UTE sequence may be used for detailed investigations of biomedical flows, for example, when studying flow patterns in a 3D-printed replica of vessels, aneurysms, or artificial heart valves.

AFFILIATIONS

¹Physikalisch-Technische Bundesanstalt (PTB), Braunschweig and Berlin, Berlin, Germany

²Department of Radiology, Charité – Universitätsmedizin Berlin, Corporate Member of Freie Universität Berlin and Humboldt-Universität zu Berlin, Berlin, Germany

³Center for Magnetic Resonance Research, University of Minnesota, Minneapolis, Minnesota, USA

⁴Division of Medical Physics in Radiology, German Cancer Research Center (DKFZ), Heidelberg, Germany

⁵Department of Medical Physics, University of Wisconsin, Madison, Wisconsin, USA

⁶Institute of Radiology, University Hospital Erlangen, Friedrich-Alexander-Universität Erlangen-Nürnberg (FAU), Erlangen, Germany

⁷Department of Radiology, University of Wisconsin Madison, Madison, Wisconsin, USA

⁸School of Imaging Science and Biomedical Engineering, King's College London, London, United Kingdom

⁹Department of Medical Engineering, Technical University of Berlin, Berlin, Germany

¹⁰Charité—Universitätsmedizin Berlin, Corporate Member of Freie Universität Berlin and Humboldt-Universität zu Berlin, Berlin, Germany

¹¹Working Group on Cardiovascular Magnetic Resonance, Experimental and Clinical Research Center, a joint cooperation between the Charité Medical Faculty and the Max-Delbrueck Center for Molecular Medicine, Berlin, Germany

¹²DZHK (German Center for Cardiovascular Research), Partner Site Berlin, Berlin, Germany

¹³Department of Cardiology and Nephrology, HELIOS Hospital Berlin-Buch, Berlin, Germany

ACKNOWLEDGEMENT

Open Access funding enabled and organized by Projekt DEAL.

FUNDING INFORMATION

Funding was provided from the German Research Foundation DFG (Deutsche Forschungsgemeinschaft) through grant/award numbers SCHM 2677/4-1 and GRK2260-BIOQIC.

ORCID

Katja Degenhardt  <https://orcid.org/0000-0002-0482-9698>

Simon Schmidt  <https://orcid.org/0000-0003-1835-4002>

Christoph S. Aigner  <https://orcid.org/0000-0003-3618-9610>

Fabian J. Kratzer  <https://orcid.org/0000-0001-7454-1641>

Max Mueller  <https://orcid.org/0000-0001-6731-9583>

Christoph Kolbitsch  <https://orcid.org/0000-0002-4355-8368>

Armin M. Nagel  <https://orcid.org/0000-0003-0948-1421>

Oliver Wieben  <https://orcid.org/0000-0002-7931-1930>

Tobias Schaeffter  <https://orcid.org/0000-0003-1310-2631>

Jeanette Schulz-Menger  <https://orcid.org/0000-0003-3100-1092>

Sebastian Schmitter  <https://orcid.org/0000-0003-4410-6790>

REFERENCES

1. Nayak KS, Nielsen JF, Bernstein MA, et al. Cardiovascular magnetic resonance phase contrast imaging. *J Cardiovasc Magn Reson*. 2015;17:71.
2. Wigström L, Sjöqvist L, Wranne B. Temporally resolved 3D phase-contrast imaging. *Magn Reson Med*. 1996;36:800-803.
3. Markl M, Frydrychowicz A, Kozerke S, Hope M, Wieben O. 4D flow MRI. *J Magn Reson Imag*. 2012;36:1015-1036.
4. Ebberts T, Wigström L, Bolger AF, Engvall J, Karlsson M. Estimation of relative cardiovascular pressures using time-resolved three-dimensional phase contrast MRI. *Magn Reson Med*. 2001;45:872-879.
5. Frydrychowicz A, Stalder AF, Russe MF, et al. Three-dimensional analysis of segmental wall shear stress in the aorta by flow-sensitive four-dimensional-MRI. *J Magn Reson Imag*. 2009;30:77-84.
6. Arvidsson PM, Töger J, Heiberg E, Carlsson M, Arheden H. Quantification of left and right atrial kinetic energy using four-dimensional intracardiac magnetic resonance imaging flow measurements. *J Appl Physiol(1985)*. 2013;114:1472-1481.
7. Wentland AL, Wieben O, François CJ, et al. Aortic pulse wave velocity measurements with undersampled 4D flow-sensitive MRI: comparison with 2D and algorithm determination. *J Magn Reson Imaging*. 2013;37:853-859.
8. Kilner PJ, Yang GZ, Mohiaddin RH, Firmin DN, Longmore DB. Helical and retrograde secondary flow patterns in the aortic arch studied by three-directional magnetic resonance velocity mapping. *Circulation*. 1993;88:2235-2247.
9. Töger J, Kanski M, Carlsson M, et al. Vortex ring formation in the left ventricle of the heart: analysis by 4D flow MRI and Lagrangian coherent structures. *Ann Biomed Eng*. 2012;40:2652-2662.
10. Bolger AF, Heiberg E, Karlsson M, et al. Transit of blood flow through the human left ventricle mapped by cardiovascular magnetic resonance. *J Cardiovasc Magn Reson*. 2007;9:741-747.
11. Zimmermann J, Loecher M, Kolawole FO, et al. On the impact of vessel wall stiffness on quantitative flow dynamics in a synthetic model of the thoracic aorta. *Sci Rep*. 2021;11:6703.
12. Amili O, Schiavazzi D, Moen S, Jagadeesan B, Van de Moortele PF, Coletti F. Hemodynamics in a giant intracranial aneurysm characterized by in vitro 4D flow MRI. *PLoS One*. 2018;13:e0188323.
13. Schmidt S, Bruschewski M, Flassbeck S, et al. Phase-contrast acceleration mapping with synchronized encoding. *Magn Reson Med*. 2021;86:3201-3210.
14. Canstein C, Cachot P, Faust A, et al. 3D MR flow analysis in realistic rapid-prototyping model systems of the thoracic aorta: comparison with in vivo data and computational fluid dynamics in identical vessel geometries. *Magn Reson Med*. 2008;59:535-546.
15. Rutkowski DR, Reeder SB, Fernandez LA, Roldán-Alzate A. Surgical planning for living donor liver transplant using 4D flow MRI, computational fluid dynamics and in vitro experiments. *Comput Methods Biomech Biomed Eng Imaging Vis*. 2018;6:545-555.
16. Biglino G, Cosentino D, Steeden JA, et al. Using 4D cardiovascular magnetic resonance imaging to validate computational fluid dynamics: a case study. *Front Pediatr*. 2015;3:107.
17. Töger J, Bidhult S, Revstedt J, Carlsson M, Arheden H, Heiberg E. Independent validation of four-dimensional flow MR velocities and vortex ring volume using particle imaging velocimetry and planar laser-induced fluorescence. *Magn Reson Med*. 2016;75:1064-1075.
18. Corrado PA, Medero R, Johnson KM, François CJ, Roldán-Alzate A, Wieben O. A phantom study comparing radial trajectories for accelerated cardiac 4D flow MRI against a particle imaging velocimetry reference. *Magn Reson Med*. 2021;86:363-371.
19. Dyverfeldt P, Bissell M, Barker AJ, et al. 4D flow cardiovascular magnetic resonance consensus statement. *J Cardiovasc Magn Reson*. 2015;17:72.
20. Steinman DA, Ethier CR, Rutt BK. Combined analysis of spatial and velocity displacement artifacts in phase contrast measurements of complex flows. *J Magn Reson Imaging*. 1997;7:339-346.
21. Hamilton CA. Effects of intravoxel velocity distributions on the complex difference method of phase-contrast MR angiography. *J Magn Reson Imaging*. 1996;6:409-410.
22. Firmin DN, Naylor GL, Kilner PJ, Longmore DB. The application of phase shifts in NMR for flow measurement. *Magn Reson Med*. 1990;14:230-241.
23. Nishimura DG, Jackson JI, Pauly JM. On the nature and reduction of the displacement artifact in flow images. *Magn Reson Med*. 1991;22:481-492.
24. Kouwenhoven M, Hofman MB, Sprenger M. Motion induced phase shifts in MR: acceleration effects in quantitative flow measurements—a reconsideration. *Magn Reson Med*. 1995;33:766-777.
25. Bakhshinejad A, Baghaie A, Vali A, Saloner D, Rayz VL, D'Souza RM. Merging computational fluid dynamics and 4D flow MRI using proper orthogonal decomposition and ridge regression. *J Biomech*. 2017;58:162-173.
26. Gupta V, Bustamante M, Fredriksson A, Carlhäll CJ, Ebberts T. Improving left ventricular segmentation in four-dimensional flow MRI using intramodality image registration for cardiac blood flow analysis. *Magn Reson Med*. 2018;79:554-560.
27. Roberts GS, Loecher MW, Spahic A, et al. Virtual injections using 4D flow MRI with displacement corrections and constrained probabilistic streamlines. *Magn Reson Med*. 2022;87:2495-2511.
28. Schmidt S, Flassbeck S, Schmelter S, Schmeier E, Ladd ME, Schmitter S. The impact of 4D flow displacement artifacts on wall shear stress estimation. *Magn Reson Med*. 2021;85:3154-3168.
29. Thunberg P, Wigström L, Ebberts T, Karlsson M. Correction for displacement artifacts in 3D phase contrast imaging: displacement artifacts in 3D PC imaging. *J Magn Reson Imaging*. 2002;16:591-597.
30. Wedeen VJ, Wendt RE III, Jerosch-Herold M. Motional phase artifacts in Fourier transform MRI. *Magn Reson Med*. 1989;11:114-120.
31. Bernstein MA, Shimakawa A, Pelc NJ. Minimizing TE in moment-nulled or flow-encoded two-and three-dimensional gradient-echo imaging. *J Magn Reson Imaging*. 1992;2:583-588.
32. Schmidt S, Flassbeck S, Bachert P, Ladd ME, Schmitter S. Velocity encoding and velocity compensation for multi-spoke RF excitation. *Magn Reson Imaging*. 2020;66:69-85.
33. Ståhlberg F, Søndergaard L, Thomsen C, Henriksen O. Quantification of complex flow using MR phase imaging—a study of

- parameters influencing the phase/velocity relation. *Magn Reson Imaging*. 1992;10:13-23.
34. Petersson S, Dyverfeldt P, Sigfridsson A, Lantz J, Carlhäll CJ, Ebbers T. Quantification of turbulence and velocity in stenotic flow using spiral three-dimensional phase-contrast MRI. *Magn Reson Med*. 2016;75:1249-1255.
 35. Bruschiowski M, Kolkmann H, John K, Grundmann S. Phase-contrast single-point imaging with synchronized encoding: a more reliable technique for in vitro flow quantification. *Magn Reson Med*. 2019;81:2937-2946.
 36. Richardson DB, MacFall JR, Sostman HD, Spritzer CE. Asymmetric-Echo, short TE, retrospectively gated MR imaging of the heart and pulmonary vessels. *J Magn Reson Imaging*. 1994;4:131-137.
 37. Kadbi M, Wang H, Negahdar M, et al. A novel phase-corrected 3D cine ultra-short TE (UTE) phase-contrast MRI technique. *Annu Int Conf IEEE Eng Med Biol Soc*. 2012;2012:77-81.
 38. Kadbi M, Negahdar M, Cha JW, et al. 4D UTE flow: a phase-contrast MRI technique for assessment and visualization of stenotic flows. *Magn Reson Med*. 2015;73:939-950.
 39. Negahdar M, Kadbi M, Kendrick M, Stoddard MF, Amini AA. 4D spiral imaging of flows in stenotic phantoms and subjects with aortic stenosis. *Magn Reson Med*. 2016;75:1018-1029.
 40. Nielles-Vallespin S, Weber MA, Bock M, et al. 3D radial projection technique with ultrashort echo times for sodium MRI: clinical applications in human brain and skeletal muscle. *Magn Reson Med*. 2007;57:74-81.
 41. Krämer M, Motaal AG, Herrmann KH, et al. Cardiac 4D phase-contrast CMR at 9.4T using self-gated ultra-short echo time (UTE) imaging. *J Cardiovasc Magn Reson*. 2017;19:1-13.
 42. Winter P, Andelovic K, Kampf T, et al. Fast self-navigated wall shear stress measurements in the murine aortic arch using radial 4D-phase contrast cardiovascular magnetic resonance at 17.6T. *J Cardiovasc Magn Reson*. 2019;21:64.
 43. Braig M, Menza M, Leupold J, et al. Analysis of accelerated 4D flow MRI in the murine aorta by radial acquisition and compressed sensing reconstruction. *NMR Biomed*. 2020;33:e4394.
 44. Vannesjo SJ, Haeberlin M, Kasper L, et al. Gradient system characterization by impulse response measurements with a dynamic field camera. *Magn Reson Med*. 2013;69:583-593.
 45. Aigner CS, Rund A, Abo Seada S, et al. Time optimal control-based RF pulse design under gradient imperfections. *Magn Reson Med*. 2020;83:561-574.
 46. Petersson S, Dyverfeldt P, Ebbers T. Assessment of the accuracy of MRI wall shear stress estimation using numerical simulations. *J Magn Reson Imaging*. 2012;36:128-138.
 47. Newling B, Poirier CC, Zhi Y, et al. Velocity imaging of highly turbulent gas flow. *Phys Rev Lett*. 2004;93:154503.
 48. Gu T, Korosec FR, Block WF, et al. PC VIPR: a high-speed 3D phase-contrast method for flow quantification and high-resolution angiography. *Am J Neuroradiol*. 2005;26:743-749.
 49. O'Brien KR, Myerson SG, Cowan BR, Young AA, Robson MD. Phase contrast ultrashort TE: a more reliable technique for measurement of high-velocity turbulent stenotic jets. *Magn Reson Med*. 2009;62:626-636.
 50. Nagel AM, Laun FB, Weber MA, Matthies C, Semmler W, Schad LR. Sodium MRI using a density-adapted 3D radial acquisition technique. *Magn Reson Med*. 2009;62:1565-1573.
 51. Gurney PT, Hargreaves BA, Nishimura DG. Design and analysis of a practical 3D cones trajectory. *Magn Reson Med*. 2006;55:575-582.
 52. Atkinson IC, Lu A, Thulborn KR. Characterization and correction of system delays and eddy currents for MR imaging with ultrashort echo-time and time-varying gradients. *Magn Reson Med*. 2009;62:532-537.

SUPPORTING INFORMATION

Additional supporting information may be found in the online version of the article at the publisher's website.

Figure S1. 3D flow measurements in a stenotic flow phantom with $VENC = 2.5$ m/s and flow rate Q_1 . (A) displays the magnitude images, (B–D) the velocity maps v_z , v_x and v_y . Slices 9, 20, 38, 120 are displayed for SYNC-SPI, Cart RO_{\parallel} , Cart RO_{\perp} and PC-UTE, respectively.

Figure S2. 3D flow measurements in a stenotic flow phantom with $VENC = 2.5$ m/s and flow rate Q_2 . (A) displays the magnitude images, (B–D) the velocity maps v_z , v_x and v_y . Slices 9, 20, 38, 120 are displayed for SYNC-SPI, Cart RO_{\parallel} , Cart RO_{\perp} and PC-UTE, respectively.

Figure S3. 3D flow measurements in a stenotic flow phantom with $VENC = 2.5$ m/s and flow rate Q_3 . (A) displays the magnitude images, (B–D) the velocity maps v_z , v_x and v_y . Slices 9, 20, 38, 120 are displayed for SYNC-SPI, Cart RO_{\parallel} , Cart RO_{\perp} and PC-UTE, respectively.

Figure S4. Magnitude images of 3D flow measurements in a stenotic flow phantom with $VENC = 2.5$ m/s and flow rates $Q_1 - Q_3$ displayed in (A–C). Slices 9, 20, 38, 120 are displayed for SYNC-SPI, Cart RO_{\parallel} , Cart RO_{\perp} and PC-UTE, respectively.

Figure S5. Slices with sagittal orientations of flow measurement with $VENC = 2.5$ m/s and flow rate Q_1 . (A) magnitude maps, (B) velocity maps v_z and velocity line plots (C) along stenosis averaged over two neighboring lines. Slices 38, 38, 102, 102 are displayed for SYNC-SPI, Cart RO_{\parallel} , Cart RO_{\perp} and PC-UTE, respectively.

Figure S6. 3D flow measurements in a stenotic flow phantom with $VENC = 2.5$ m/s and flow rate Q_1 for Cart RO_{\parallel} and Cart RO_{\perp} with varying isotropic resolutions (0.6/1.6/1.8/2.3/2.7 mm), slices 20/6/6/5/4 are shown for Cart RO_{\parallel} and slices 19/8/7/6/5 for Cart RO_{\perp} .

Figure S7. Velocity component v_z of 3D flow measurements with Cart RO_{\parallel} and Cart RO_{\perp} (Figure S6) in a stenotic flow phantom with $VENC = 2.5$ m/s and flow rate Q_1 for isotropic resolutions: 0.6/1.6/1.8/2.3/2.7 mm.

Figure S8. Mean velocity (A) and volumetric flow rate (B) of 3D flow measurement in a stenotic flow phantom with $VENC = 2.5$ m/s and flow rate Q_1 obtained from cross-sectional areas at different positions in flow phantom: pipe inflow, outflow 1, stenosis, outflow 2.

Figure S9. (A) Magnitude maps of PC-UTE acquisition from flow measurement with $VENC = 2.5$ m/s and flow rate Q_1 . (B) Velocities v_z along dashed white line in (A) for PC-UTE data reconstructed with: (i) nominal, (ii) GIRF-corrected trajectory and (iii) after background (b.g.) phase correction applied on (ii).

Table S1. Acquisition parameters of 3D flow measurements with constant flow rates $Q_1 - Q_3$. Number of slices correspond to PE_2 -steps in Cartesian and SYNC-SPI and to base resolution in PC-UTE acquisition: 26, 60, 60, 256 slices for SYNC-SPI, Cart RO_{\parallel} , Cart RO_{\perp} and PC-UTE, respectively.

Table S2. Acquisition parameters of 3D flow measurements with constant flow rate Q_1 for Cart RO_{\parallel} and

Cart RO_{\perp} with varying isotropic resolutions (0.6/1.6/1.8/2.3/2.7 mm). Number of slices in Cartesian acquisitions: (40/14/14/12/10) for Cart RO_{\parallel} and (40/16/14/12/10) for Cart RO_{\perp} , respectively to the resolution.

How to cite this article: Degenhardt K, Schmidt S, Aigner CS, et al. Toward accurate and fast velocity quantification with 3D ultrashort TE phase-contrast imaging. *Magn Reson Med*. 2024;91:1994-2009. doi: 10.1002/mrm.29978